(Preprint) AAS AAS XX-XXX

EJECTION COLLISION ORBITS IN THE SPATIAL RESTRICTED 3-BODY PROBLEM

Joan Gimeno[*], J. D. Mireles James[†], and Luke T. Peterson[‡]

Ejection and collision trajectories play a fundamental role in the transport geometry of cislunar space. We study these trajectories in the spatial circular restricted three-body problem using Kustaanheimo–Stiefel regularization, which replaces each singularity with a smooth ejection/collision manifold. For each selected Jacobi constant, each primary, and both time directions, we sample a Chebyshev grid of regularized ejection directions and classify the resulting trajectories as bounded, escaping, self-returning, or cross-primary colliding. The survey reveals a strong asymmetry between the two primaries: Earth-regularized ejections are predominantly return-dominated over the tested range, while Moon-regularized ejections undergo a clear transition from escape-dominated behavior to bounded return as C approaches the exterior-neck threshold C_{L_2}. Classification maps on the KS parameter domain show coherent bands, islands, and collision regions, indicating organized phase-space structure rather than random scattering. These results provide a regularized global map of near-primary ejection outcomes and a foundation for extracting structured ejection-collision connections in the Earth–Moon environment.

INTRODUCTION

The Earth–Moon region is one of the most important dynamical environments for modern spaceflight. It contains a rich network of natural transport channels, bounded motion, temporary capture, close approaches, impacts, and escape routes. These behaviors are organized by the geometry of the circular restricted three-body problem (CR3BP), where the Jacobi integral constrains the motion to Hill regions whose topology changes at the critical values associated with the libration points.[1] Near the collinear libration points, the opening and closing of the zero-velocity necks provides a global mechanism for transitions between lunar, terrestrial, and exterior realms.[2] Understanding how these transitions are reflected in families of near-primary trajectories is therefore a useful step toward a more complete description of cislunar transport.

The dynamical-systems approach has become a central tool in the study of low-energy motion in multi-body gravitational fields. Conley's analysis of low-energy transit orbits showed that phase-space structures near the collinear libration points organize transport in the restricted three-body problem.[3] Subsequent work connected this geometric viewpoint with mission design by using stable and unstable invariant manifolds of periodic and quasi-periodic libration-point orbits to construct transfers and to understand transport between different regions of the Earth–Moon and Sun–

[*]Departament de Matemàtiques i Informàtica, Universitat de Barcelona, Gran Via de les Corts Catalanes 585, 08007 Barcelona, Spain.
[†]Department of Mathematics and Statistics, Florida Atlantic University, 777 Glades Road, Boca Raton, FL 33431.
[‡]Department of Aerospace Engineering & Engineering Mechanics, University of Texas at Austin, 2617 Wichita Street, Austin, TX 78712.

Earth systems.[2,4,5] Ballistic-capture and weak-stability-boundary methods further demonstrated that multi-body dynamics can be exploited to design lunar transfers with favorable energetic and geometric properties.[6] Together, these developments show that global phase-space structure is a practical organizing principle for cislunar trajectory analysis.

This perspective is especially timely in the context of renewed lunar activity and sustained cislunar operations. Near-rectilinear halo orbits (NRHOs), which arise from the three-dimensional libration-point dynamics of the Earth–Moon system, have been studied as favorable orbits for lunar infrastructure because of their geometry, visibility, and accessibility properties.[7,8] Gateway-class mission designs operate in this same dynamical setting, where transport between Earth, lunar orbit, the lunar surface, and the exterior region is shaped by invariant structures and energy thresholds of the CR3BP.[9,10] The present work contributes to this broader picture by mapping how ejection directions from the primaries are partitioned into bounded, escaping, self-returning, and cross-primary collision outcomes. Such information is relevant to transfer accessibility, disposal and impact trajectory design, and the geometric organization of near-Moon transport.

A complementary way to study this environment is to begin at collision or ejection from a primary and ask how the corresponding trajectories populate the global phase space. For a fixed Jacobi constant, the set of regularized ejection directions forms a natural initial-condition manifold. Classifying the forward and backward evolution of this set gives a direct picture of which directions remain bounded, which escape through open gateways, and which reach the other primary. As the Jacobi constant varies, these classifications reveal how the near-primary ejection geometry responds to changes in Hill-region topology. This produces a survey-level view of transport that complements the targeted construction of individual transfers along selected invariant manifolds.

The main technical challenge is the singularity of the CR3BP vector field at the primaries. Kustaanheimo–Stiefel (KS) regularization resolves this singularity in the spatial problem by lifting the dynamics to four regularized coordinates and introducing a time transformation.[11–13] In the regularized variables, collision with the selected primary becomes a smooth set rather than a singular endpoint. This makes it possible to initialize trajectories directly on the collision/ejection manifold, propagate them through near-collision events, and classify their global outcomes in a numerically stable coordinate system. The Hopf-fibration structure of the KS map also provides a natural interpretation of the two-parameter sampling used to represent physical ejection directions.[14] Recent applications of KS regularization to close-encounter dynamics further support its usefulness for resolving near-primary motion in restricted three-body models.[15,16]

In this paper we use KS regularization to perform a Jacobi-constant survey of ejection-collision (EC) dynamics in the spatial Earth–Moon CR3BP. For each selected value of the Jacobi constant, for each regularized primary, and for both time directions (forward for ejection, backward for collision), we sample a Chebyshev grid on a Hopf slice of the KS ejection sphere. Each initial condition is integrated in regularized time and classified according to its observed outcome: escape to the exterior region, collision with the non-regularized primary, return to the regularized primary, or bounded evolution over the integration horizon. The resulting data are summarized both as aggregate outcome percentages and as classification maps on the KS parameter domain. The maps retain the geometry of the sampled ejection set and reveal coherent structures that are not visible from percentages alone.

The computations show a strong asymmetry between the two primaries over the sampled Jacobi range. Ejections from the larger primary are predominantly return-dominated in the tested cases.

Ejections from the smaller primary exhibit a clear transition from escape-dominated behavior at lower C to bounded or return-dominated behavior as C approaches the exterior-neck threshold C_{L_2}. This transition is consistent with the zero-velocity topology: as C increases toward C_{L_2}, the exterior gateway near L_2 closes and escape trajectories disappear from the sampled ejection domain. The corresponding KS-domain maps display organized bands, caps, and islands, indicating that the outcome regions are structured by the geometry of the regularized phase space.

The contribution of this work is a regularized, energy-parametrized map of near-primary ejection outcomes in the spatial Earth–Moon problem. By combining KS regularization, Chebyshev sampling, event classification, and Jacobi-constant continuation, the study provides a systematic view of how collision/ejection directions are organized across dynamically significant energy levels. This information supports the identification of cross-primary connection regions, near-miss families, escape corridors, and bounded return structures. It also provides a foundation for higher-resolution studies of specific ejection-collision connections and for future extensions to higher-fidelity cislunar models.

The remainder of the paper is organized as follows. We first review the spatial Earth–Moon CR3BP, the Jacobi integral, and the zero-velocity topology. We then present the KS regularization, its constraint structure, and the parametrization of the ejection sphere. Next, we describe the Chebyshev sampling, regularized integration, event detection, and classification procedure. The results report the Jacobi sweep through aggregate statistics, KS-domain classification maps, closest-approach diagnostics, and cross-primary collision data. We then discuss the geometric meaning of the observed transition and close with conclusions and natural directions for continued development.

DYNAMICAL MODEL

Equations of Motion

The spatial circular restricted three-body problem models the motion of a massless particle under the gravitational attraction of two massive primaries moving on circular orbits about their common barycenter. We work in the rotating synodic frame and use normalized units in which the total mass, the gravitational constant, and the mean motion are all equal to one. Let $\mu \in (0, \frac{1}{2}]$ denote the mass of the smaller primary, so the larger primary has mass $1 - \mu$.

Following the convention used in the companion EC work, we place the larger primary M_1 at $x_{M_1} = \mu$ and the smaller primary M_2 at $x_{M_2} = \mu - 1$ on the x-axis.[17,18] For the Earth-Moon system we use

$$\mu \stackrel{\text{def}}{=} \mu_{\text{EM}} = 0.0121505856093. \tag{1}$$

The equations of motion in the synodic frame are

$$\ddot{x} - 2\dot{y} = \frac{\partial \Omega}{\partial x}, \qquad \ddot{y} + 2\dot{x} = \frac{\partial \Omega}{\partial y}, \qquad \ddot{z} = \frac{\partial \Omega}{\partial z}, \tag{2}$$

where

$$\Omega(x, y, z) = \frac{1}{2}(x^2 + y^2) + \frac{1-\mu}{r_1} + \frac{\mu}{r_2},$$

and

$$r_1 = \|(x - x_{M_1}, y, z)\|, \qquad r_2 = \|(x - x_{M_2}, y, z)\|. \tag{3}$$

The vector field is singular at the primary locations.

Jacobi Constant and Zero-Velocity Topology

The CR3BP admits the Jacobi integral

$$C = 2\Omega(x, y, z) - (\dot{x}^2 + \dot{y}^2 + \dot{z}^2). \tag{4}$$

For fixed C, the motion is restricted to the region $\{2\Omega \geq C\}$, and its boundary $\{2\Omega = C\}$ is the zero-velocity surface. The topology of this surface changes at the Lagrangian critical values. For the Earth-Moon mass ratio, the values relevant to the present sweep are

$$C_{L_1} = 3.18834, \qquad C_{L_2} = 3.17216, \qquad C_{L_3} = 3.01215, \qquad C_{L_4} = C_{L_5} = 2.98800. \tag{5}$$

For $C > C_{L_1}$ the two primary lobes are disconnected. When C decreases through C_{L_1}, the L_1 neck opens and interior transit between the two lobes becomes topologically possible. Decreasing further through C_{L_2} opens the exterior gateway. The threshold C_{L_3} controls the accessibility of additional global channels. These transitions are the topological backdrop for the statistical behavior observed in the sweep.

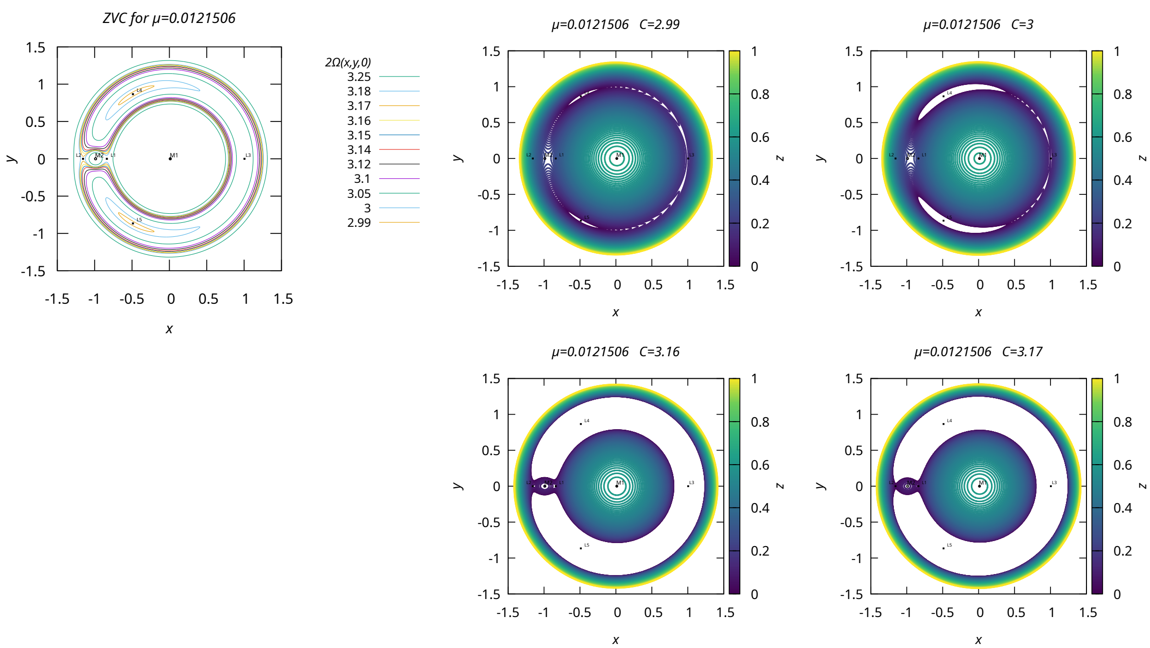

Figure 1. Zero-velocity geometry for the Earth–Moon CR3BP. The left panel shows planar zero-velocity curves for several Jacobi levels, including the critical values C_{L_1}, C_{L_2}, C_{L_3}, and $C_{L_4} = C_{L_5}$. The remaining panels show representative admissible regions in the plane $z = 0$ for selected values of C. As C increases toward $C_{L_2} \approx 3.17216$, the exterior gateway near L_2 narrows and eventually closes, providing the global topological mechanism behind the loss of escape trajectories observed in the Moon-regularized sweep.

KUSTAANHEIMO-STIEFEL REGULARIZATION

We regularize around one primary at a time. The construction is standard, so for the purposes of this proceedings paper we record the final primary-dependent model, the constraint quantities that are monitored numerically, and the explicit projection back to synodic variables. For background on spatial KS regularization, see the following classic works.[7,11–13]

Primary-Centered Coordinates and Regularized Time

Fix a primary M_i. We use the primary-dependent parameters

$$\mu_{\mathtt{KS}} = \begin{cases} \mu, & \text{regularization about } M_1, \\ 1-\mu, & \text{regularization about } M_2, \end{cases} \qquad \sigma_{\mathtt{KS}} = \begin{cases} +1, & \text{regularization about } M_1, \\ -1, & \text{regularization about } M_2. \end{cases} \tag{6}$$

The primary-centered and synodic x-coordinates are related by

$$x = x_* + \sigma_{\mathtt{KS}}\mu_{\mathtt{KS}}, \qquad \text{or equivalently} \qquad x_* = x - \sigma_{\mathtt{KS}}\mu_{\mathtt{KS}}. \tag{7}$$

Let

$$r = \sqrt{x_*^2 + y^2 + z^2}$$

denote the distance to the chosen primary. Regularized time τ is then introduced by

$$\frac{dt}{d\tau} = r. \tag{8}$$

This time regularization will remove the inverse-distance singularity from the equations of motion. Writing $u' = du/d\tau$, the regularized state is

$$(u, v, t) = (u_1, u_2, u_3, u_4, v_1, v_2, v_3, v_4, t) \in \mathbb{R}^9, \qquad u' = v.$$

KS Coordinates and Projection to Synodic Variables

The KS map lifts the re-centered position $\bar{R} = (x_*, y, z, 0)^\top \in \mathbb{R}^4$ to regularized coordinates $u = (u_1, u_2, u_3, u_4)^\top \in \mathbb{R}^4$ by

$$\bar{R} = L(u)\, u,$$

with

$$L(u) = \begin{pmatrix} u_1 & -u_2 & -u_3 & u_4 \\ u_2 & u_1 & -u_4 & -u_3 \\ u_3 & u_4 & u_1 & u_2 \\ u_4 & -u_3 & u_2 & -u_1 \end{pmatrix}. \tag{9}$$

and the identities

$$\bar{R} = L(u)u, \qquad L(u)^\top L(u) = |u|^2 I_4, \qquad r = |u|^2. \tag{10}$$

Expanding $\bar{R} = L(u)u$ gives the explicit KS-to-primary-centered position map

$$x_* = u_1^2 - u_2^2 - u_3^2 + u_4^2, \quad y = 2(u_1u_2 - u_3u_4), \quad z = 2(u_1u_3 + u_2u_4). \tag{11}$$

The synodic x-coordinate is then recovered from (7). For $r > 0$, differentiation of $\bar{R} = L(u)u$ and (8) yields the velocity reconstruction

$$(\dot{x}_*, \dot{y}, \dot{z}, 0)^\top = \frac{2}{r} L(u)v. \tag{12}$$

Equivalently, if

$$\begin{aligned} A_x &= u_1v_1 - u_2v_2 - u_3v_3 + u_4v_4, \\ A_y &= u_2v_1 + u_1v_2 - u_4v_3 - u_3v_4, \\ A_z &= u_3v_1 + u_4v_2 + u_1v_3 + u_2v_4, \end{aligned} \tag{13}$$

then

$$\dot{x} = \frac{2A_x}{r}, \qquad \dot{y} = \frac{2A_y}{r}, \qquad \dot{z} = \frac{2A_z}{r}. \tag{14}$$

These formulas are the ones used to classify trajectories in physical space: Earth and Moon impacts are detected from the reconstructed synodic distances r_1 and r_2, while escape is detected from the reconstructed synodic radius.

Explicit Regularized Model, Constraints, and the Ejection Sphere

Using the primary convention (6), the KS position map (11), the primary-centered shift (7), and the identity $r = |u|^2$, define

$$\begin{aligned}
r &= u_1^2 + u_2^2 + u_3^2 + u_4^2, \\
x_* &= u_1^2 - u_2^2 - u_3^2 + u_4^2, \\
y &= 2(u_1u_2 - u_3u_4), \\
z &= 2(u_1u_3 + u_2u_4), \\
\rho^2 &= (x_* + \sigma_{\mathtt{KS}})^2 + y^2 + z^2, \qquad \rho^{-3} = (\rho^2)^{-3/2}, \\
h_{\mathtt{KS}} &= \frac{\mu_{\mathtt{KS}}\,\rho^2\rho^{-3}}{2} + \frac{(x_* + \sigma_{\mathtt{KS}}\mu_{\mathtt{KS}})^2 + y^2}{4} - \frac{C}{4}, \\
F_{12} &= \frac{x_* + \sigma_{\mathtt{KS}}\mu_{\mathtt{KS}} - \mu_{\mathtt{KS}}\rho^{-3}(x_* + \sigma_{\mathtt{KS}})}{2}, \\
F_{22} &= \frac{y - \mu_{\mathtt{KS}}\rho^{-3}y}{2}, \\
F_{32} &= -\frac{\mu_{\mathtt{KS}}\rho^{-3}z}{2}.
\end{aligned} \tag{15}$$

Then the regularized ODE is

$$\begin{aligned}
&u_1' = v_1,\ u_2' = v_2,\ u_3' = v_3,\ u_4' = v_4, \\
&v_1' = 2(u_1^2 + u_2^2)v_2 + 2(u_2u_3 - u_1u_4)v_3 - zv_4 + h_{\mathtt{KS}}u_1 + r(F_{12}u_1 + F_{22}u_2 + F_{32}u_3), \\
&v_2' = -2(u_1^2 + u_2^2)v_1 + zv_3 + 2(u_2u_3 - u_1u_4)v_4 + h_{\mathtt{KS}}u_2 + r(F_{22}u_1 - F_{12}u_2 + F_{32}u_4), \\
&v_3' = 2(u_1u_4 - u_2u_3)v_1 - zv_2 + 2(u_3^2 + u_4^2)v_4 + h_{\mathtt{KS}}u_3 + r(F_{32}u_1 - F_{12}u_3 - F_{22}u_4), \\
&v_4' = zv_1 + 2(u_1u_4 - u_2u_3)v_2 - 2(u_3^2 + u_4^2)v_3 + h_{\mathtt{KS}}u_4 + r(F_{32}u_2 - F_{22}u_3 + F_{12}u_4), \\
&t' = r.
\end{aligned} \tag{16}$$

Origin Stability and Parametrization

The linearized KS dynamics at the origin, i.e. $r = 0$, is controlled by $h_{\mathtt{KS}}(0)$, and the eigenvalues satisfy

$$\lambda^2 = h_{\mathtt{KS}}(0) = \mu_{\mathtt{KS}}/2 + \mu_{\mathtt{KS}}^2/4 - C/4.$$

Let $C_i^* = 2\mu_{\mathtt{KS}} + \mu_{\mathtt{KS}}^2$. For $C > C_i^*$ the origin is elliptic. In the Earth-Moon system the present sweep lies above both thresholds C_1^* and C_2^*, so both regularized origins are in the center regime throughout. This observation matters later when we interpret coherent ok-islands in the Moon classification maps as footprints of near-collision periodic families rather than numerical artifacts.

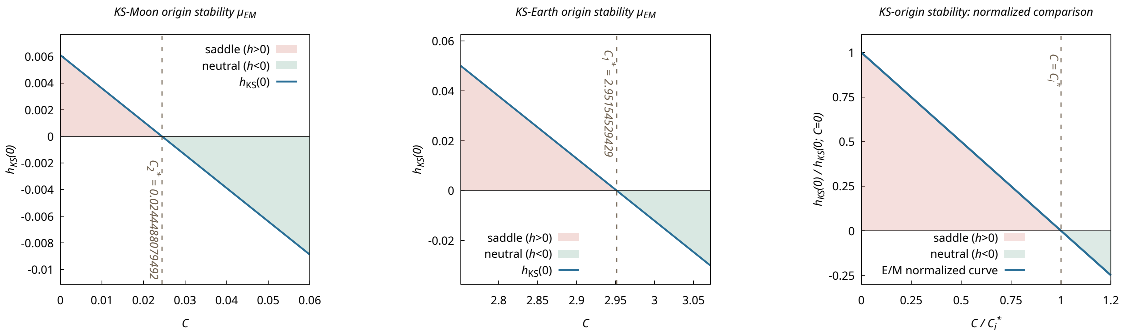

Figure 2. Linear stability of the regularized KS origin for Earth- and Moon-centered regularization. The sign of $h_{\mathrm{KS}}(0)$ determines the local type of the origin: for $C < C_i^*$, one has $h_{\mathrm{KS}}(0) > 0$ and the linearized origin is saddle-type, while for $C > C_i^*$, one has $h_{\mathrm{KS}}(0) < 0$ and the origin is elliptic, or center-type. The Earth and Moon thresholds differ strongly in physical C, but collapse to the same linear transition curve after normalization by C_i^*.

KS first integrals

On the physical constraint manifold, the regularized dynamics admits the KS quantities

$$g_{\mathrm{KS}} = u_4 v_1 - u_3 v_2 + u_2 v_3 - u_1 v_4, \qquad E_{\mathrm{KS}} = |v|^2 - r\, h_{\mathrm{KS}} - \frac{1-\mu_{\mathrm{KS}}}{2} \tag{17}$$

which vanish on physical trajectories. A numerically balanced residual is

$$R_{\mathrm{KS}} = r\, E_{\mathrm{KS}} - g_{\mathrm{KS}}^2. \tag{18}$$

Near $r = 0$, the pair $(g_{\mathrm{KS}}, E_{\mathrm{KS}})$ is scale-mismatched while R_{KS} remains a useful defect monitor.

Proposition 1. *For the exact flow of* (16)*, g_{KS} and E_{KS} are first integrals:*

$$\frac{d}{d\tau} g_{\mathrm{KS}} = 0, \qquad \frac{d}{d\tau} E_{\mathrm{KS}} = 0. \tag{19}$$

Proof. We prove the two identities separately.

1) Phase-fixing first integral. Differentiate g_{KS} from (17):

$$\begin{aligned} g'_{\mathrm{KS}} &= u'_4 v_1 + u_4 v'_1 - u'_3 v_2 - u_3 v'_2 + u'_2 v_3 + u_2 v'_3 - u'_1 v_4 - u_1 v'_4 \\ &= v_4 v_1 - v_3 v_2 + v_2 v_3 - v_1 v_4 + u_4 v'_1 - u_3 v'_2 + u_2 v'_3 - u_1 v'_4 \\ &= u_4 v'_1 - u_3 v'_2 + u_2 v'_3 - u_1 v'_4. \end{aligned}$$

Insert v'_i from (16). Terms split into three groups.

Gyroscopic terms (those linear in v without h_{KS}, F_{ij}) cancel pairwise by direct expansion. h_{KS}-terms cancel identically:

$$u_4(h_{\mathrm{KS}} u_1) - u_3(h_{\mathrm{KS}} u_2) + u_2(h_{\mathrm{KS}} u_3) - u_1(h_{\mathrm{KS}} u_4) = 0.$$

For rF-terms, substitute and group by F_{12}, F_{22}, F_{32}:

$$\begin{aligned} &u_4(F_{12}u_1 + F_{22}u_2 + F_{32}u_3) - u_3(F_{22}u_1 - F_{12}u_2 + F_{32}u_4) \\ &\quad + u_2(F_{32}u_1 - F_{12}u_3 - F_{22}u_4) - u_1(F_{32}u_2 - F_{22}u_3 + F_{12}u_4) = 0. \end{aligned}$$

Hence $g'_{\mathtt{KS}} = 0$.

2) Energy first integral. Differentiate $E_{\mathtt{KS}}$ from (17):

$$E'_{\mathtt{KS}} = 2\mathbf{v} \cdot \mathbf{v}' - r' h_{\mathtt{KS}} - r h'_{\mathtt{KS}}. \tag{20}$$

From $r = \|\mathbf{u}\|^2$, $r' = 2\mathbf{u} \cdot \mathbf{v}$. Write $\mathbf{v}'$ as

$$\mathbf{v}' = A(\mathbf{u})\mathbf{v} + h_{\mathtt{KS}}\, \mathbf{u} + r\, \mathbf{G},$$

where $A(\mathbf{u})$ is the gyroscopic skew-symmetric part and

$$\begin{aligned} G_1 &= F_{12}u_1 + F_{22}u_2 + F_{32}u_3, \quad G_3 = F_{32}u_1 - F_{12}u_3 - F_{22}u_4, \\ G_2 &= F_{22}u_1 - F_{12}u_2 + F_{32}u_4, \quad G_4 = F_{32}u_2 - F_{22}u_3 + F_{12}u_4. \end{aligned}$$

Since $A^\top = -A$, one has $\mathbf{v} \cdot A\mathbf{v} = 0$. Therefore

$$2\mathbf{v} \cdot \mathbf{v}' = 2h_{\mathtt{KS}}\, \mathbf{u} \cdot \mathbf{v} + 2r\, \mathbf{v} \cdot \mathbf{G} = r' h_{\mathtt{KS}} + 2r\, \mathbf{v} \cdot \mathbf{G}. \tag{21}$$

Plug (21) into (20):

$$E'_{\mathtt{KS}} = 2r\, \mathbf{v} \cdot \mathbf{G} - r h'_{\mathtt{KS}}. \tag{22}$$

So it remains to prove

$$h'_{\mathtt{KS}} = 2\, \mathbf{v} \cdot \mathbf{G}. \tag{23}$$

Also, by direct expansion of $\mathbf{v} \cdot \mathbf{G}$:

$$\mathbf{v} \cdot \mathbf{G} = F_{12}A_x + F_{22}A_y + F_{32}A_z, \tag{24}$$

where A_x, A_y, and A_z are those in (13). Using (14):

$$\mathbf{v} \cdot \mathbf{G} = \frac{1}{2}\big(F_{12}x'_* + F_{22}y' + F_{32}z'\big). \tag{25}$$

Substitute $F_{12} = \frac{x_* + \sigma_{\mathtt{KS}}\mu_{\mathtt{KS}} - \mu_{\mathtt{KS}}\rho^{-3}x_1}{2}$, $F_{22} = \frac{y - \mu_{\mathtt{KS}}\rho^{-3}y}{2}$, $F_{32} = -\frac{\mu_{\mathtt{KS}}\rho^{-3}z}{2}$:

$$2\, \mathbf{v} \cdot \mathbf{G} = \frac{1}{2}\Big(xx' + yy' - \mu_{\mathtt{KS}}\rho^{-3}(x_1 x'_* + yy' + zz')\Big).$$

Now $x_1 = x_* + \sigma_{\mathtt{KS}}$ and $x = x_* + \sigma_{\mathtt{KS}}\mu_{\mathtt{KS}}$, so $x'_1 = x'_* = x'$. Hence

$$x_1 x' + yy' + zz' = \frac{(\rho^2)'}{2}.$$

Therefore

$$2\, \mathbf{v} \cdot \mathbf{G} = \frac{1}{2}(xx' + yy') - \frac{\mu_{\mathtt{KS}}}{4\rho^3}(\rho^2)'. \tag{26}$$

On the other hand,

$$h_{\mathtt{KS}} = \frac{\mu_{\mathtt{KS}}\rho^2\rho^{-3}}{2} + \frac{x^2 + y^2}{4} - \frac{C}{4},$$

so

$$h'_{\mathtt{KS}} = -\frac{\mu_{\mathtt{KS}}}{4\rho^3}(\rho^2)' + \frac{1}{2}((x_* + \sigma_{\mathtt{KS}}\mu_{\mathtt{KS}})x'_* + yy'). \tag{27}$$

Comparing (26) and (27) yields (23). Then (22) gives $E'_{\mathtt{KS}} = 0$. $\square$

Figure 3 shows similar version of Figure 1 but from KS conditions.

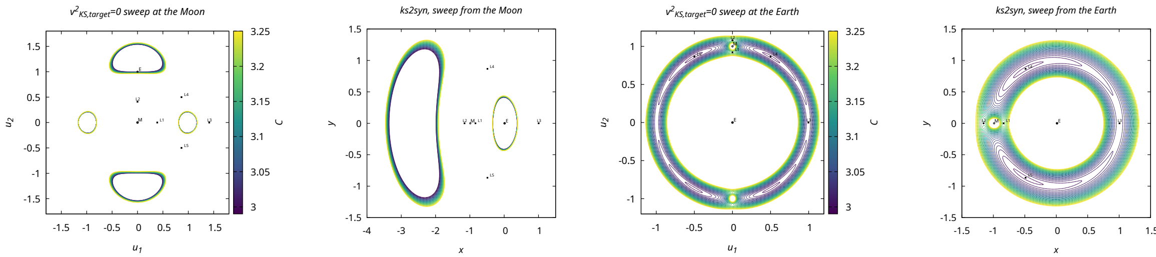

Figure 3. Boundary-level representation of admissible KS initial conditions and their projection to synodic coordinates. The Moon-regularized and Earth-regularized panels show contours of $v^2_{\mathtt{KS},\mathrm{target}} = rh_{\mathtt{KS}} + (1-\mu_{\mathtt{KS}})/2$ over the KS parameter plane, together with the corresponding images in physical synodic coordinates. The deformation of these contours as C varies illustrates how the regularized ejection set maps into the physical zero-velocity geometry for each primary.

Ejection-Collision set

At exact collision with the regularized primary one has $u = 0$, and the energy constraint reduces to

$$|v|^2 = \frac{1-\mu_{\mathtt{KS}}}{2} =: K_i. \tag{28}$$

Thus the set of ejection velocities is the sphere

$$\mathcal{O}_i = \{v \in \mathbb{R}^4 : |v|^2 = K_i\} \cong S^3. \tag{29}$$

Forward advection of $\mathcal{O}_i$ in regularized time gives the ejection manifold, and backward advection gives the collision manifold.

Parametrization of the E/C set To sample $\mathcal{O}_i$ we use the base of the Hopf fibration by fixing the fiber angle and parametrizing the sphere with two angles $\theta_1 \in [\pi/2, 3\pi/2]$ and $\theta_2 \in [0, \pi]$:

$$\begin{aligned} v_1 &= \sqrt{K_i}\cos\tfrac{\theta_1}{2}\sin\theta_2, \quad v_3 = \sqrt{K_i}\cos\tfrac{\theta_1}{2}\cos\theta_2, \\ v_2 &= \sqrt{K_i}\sin\tfrac{\theta_1}{2}\sin\theta_2, \quad v_4 = -\sqrt{K_i}\sin\tfrac{\theta_1}{2}\cos\theta_2. \end{aligned} \tag{30}$$

This is the two-parameter reference domain. The Hopf-fibration viewpoint is particularly useful here because it clarifies why a two-parameter slice of the KS velocity sphere still captures the full physical ejection set modulo the fiber symmetry.[14] In the computations below, the Chebyshev nodes are first generated on the normalized square $(\sigma_1, \sigma_2) \in [0,1]^2$ and then mapped to the angular variables (θ_1, θ_2). Each point of the square therefore corresponds to one regularized ejection direction from the selected primary, see Figure 4 for an illustration.

NUMERICAL METHODOLOGY

This section describes the numerical procedure used to generate the ejection-collision classification data. The computations are performed in Kustaanheimo–Stiefel (KS) regularized coordinates, with one primary regularized at a time. The regularization index is denoted by p: $p = 1$ corresponds to Earth regularization and $p = 2$ corresponds to Moon regularization. The integration direction is denoted by d, with $d = +1$ corresponding to forward-time integration and $d = -1$ corresponding to backward-time integration.

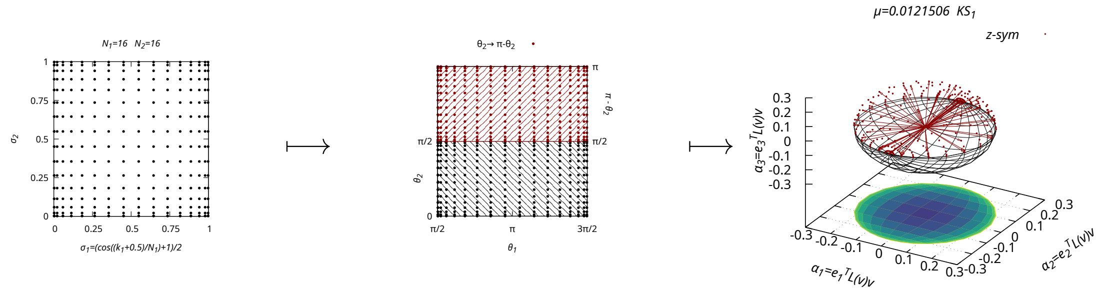

Figure 4. Construction of the sampled ejection-collision set. A tensor-product Chebyshev grid on the normalized square $(\sigma_1, \sigma_2) \in [0,1]^2$ is mapped to the Hopf-slice angular domain $(\theta_1, \theta_2) \in [\pi/2, 3\pi/2] \times [0, \pi]$, which parametrizes the KS collision velocity sphere O_i. The right panel shows the corresponding projected ejection directions $a = L(v)v$. The symmetry $\theta_2 \mapsto \pi - \theta_2$ indicates the reflected z-directions represented within the same two-parameter sampling domain.

For each value of the Jacobi constant C, each regularized primary $p \in \{1,2\}$, and each integration direction $d \in \{+1,-1\}$, a two-dimensional grid of ejection initial conditions is constructed on the KS collision manifold. Each initial condition is then integrated in regularized time until it either reaches the non-regularized primary, escapes beyond a prescribed large-radius threshold, or reaches the end of the integration horizon without triggering either event. The final output is a classification map on the KS ejection domain, together with aggregate percentages of collision, escape, and bounded outcomes.

Regularized Initial Conditions

The KS formulation removes the singularity at the selected primary by replacing collision with a smooth regularized set. At exact collision with the regularized primary, the KS position satisfies $u = 0$, while the KS velocity $v \in \mathbb{R}^4$ lies on a three-sphere determined by the energy constraint, $\mathcal{O}_p$ in (29).

The ejection sphere is sampled using a two-angle Hopf slice. For each pair $(\theta_1, \theta_2) \in [\pi/2, 3\pi/2] \times [0, \pi]$, the initial KS state is $u(0) = 0$, and $v(0)$ as in (30). The physical time variable is initialized as $t(0) = 0$. These initial conditions represent ejections from the selected regularized primary. Integrating the same set in the negative time direction gives the corresponding collision-manifold and forward the ejection-manifold.

Chebyshev Sampling of the Ejection Domain

The parameter domain $[\pi/2, 3\pi/2] \times [0, \pi]$ is sampled with a tensor-product Chebyshev grid. For a mesh size $N_1 \times N_2$, the reference nodes are DCT-II nodes,

$$\alpha_k = \cos\left(\frac{\pi(k+1/2)}{N}\right), \qquad k = 0, \ldots, N-1.$$

These nodes are then affinely mapped from $[-1,1]$ to the desired angular intervals. This gives (θ_1, θ_2). The main scans use both 64×64 and 128×128 meshes. The 64×64 data are useful because they sample the transition region in C more densely, while the 128×128 data provide cleaner spatial boundaries in the classification maps. Each 64×64 case contains 4096 initial conditions, and each 128×128 case contains 16384 initial conditions.

For plotting, the angular variables are also converted to normalized coordinates

$$\sigma_1, \sigma_2 \in [0, 1],$$

where σ_1 and σ_2 correspond respectively to the sampled directions in θ_1 and θ_2. The classification maps are therefore displayed on the square $[0, 1]^2$, but each point represents a KS ejection velocity on the regularized collision sphere.

Jacobi-Constant Sweep

The computations are organized as a sweep in the Jacobi constant C. The sampled values include both coarse values over the full range and refined values near the exterior-neck threshold C_{L_2}. The data used in the current classification figures include

$$\begin{aligned} C \in \{&2.70, 2.75, 2.80, 2.85, 2.90, 2.95, 2.99, 3.05, 3.10, 3.15, \\ &3.16, 3.168, 3.170, 3.171, 3.172, 3.173, 3.174, 3.175, 3.176\}. \end{aligned}$$

This interval covers the transition from escape-dominated Moon ejections at low C to almost entirely bounded Moon ejections near and above C_{L_2}. The Earth-Moon critical value

$$C_{L_2} \approx 3.17216$$

is especially important because it corresponds to the closing of the exterior gateway. The refined values between $C = 3.168$ and $C = 3.176$ were therefore included to locate the final disappearance of the residual escape set.

For each C, four cases are computed:

$$(p, d) \in \{(1, +1), (1, -1), (2, +1), (2, -1)\}.$$

Thus each Jacobi value includes Earth-regularized forward integration, Earth-regularized backward integration, Moon-regularized forward integration, and Moon-regularized backward integration.

Time Integration

Each initial condition is propagated using the KS-regularized equations of motion. The integration is performed in regularized time, not directly in physical time. Physical time is included as a state variable and evolves according to the Sundman time transformation (8). This distinction matters because the code parameter called `maxtime` is the terminal value of the independent integration variable used by the KS integrator.

The implementation uses a variable-step Taylor method based on the approach of.[19] The integration direction is imposed by setting the final regularized time to

$$\tau_f = d\,\tau_{\max},$$

where $d = +1$ gives forward integration and $d = -1$ gives backward integration. The Taylor stepper is also passed the same direction sign. The absolute and relative tolerances are controlled by logarithmic input parameters, denoted in the code by `log10abs` and `log10rel` with default values -16.

The default integration horizon in the current code is $\tau_{\max} = 10^4$.

Event Detection and Classification

At each accepted integration step, the KS state is projected back to synodic CR3BP coordinates. The reconstructed physical position and velocity are used to evaluate distances to the Earth and Moon and to determine whether an event has occurred.

Three terminal outcomes are used.

First, a cross-primary collision is recorded if the trajectory reaches the non-regularized primary. The collision threshold is

$$r_{\mathrm{col}} = 0.05$$

for both primaries in the current runs. Thus, if the computation is Earth-regularized, a collision event means that the trajectory reaches the Moon; if the computation is Moon-regularized, a collision event means that the trajectory reaches the Earth. These are the transfer-relevant ejection-collision events.

Second, an escape is recorded if the reconstructed synodic trajectory reaches the large-distance threshold

$$R_{\mathrm{esc}} = 10^3.$$

At this scale, the distinction between distance from the barycenter and distance from either primary is negligible for the purposes of classification.

Third, a trajectory is classified as bounded over the integration horizon if neither cross-primary collision nor escape occurs before $\tau = \tau_f$.

Self-return to the regularized primary is treated differently from cross-primary collision. Since the selected primary has been regularized, the KS flow remains smooth through $u = 0$. Therefore, a return to the regularized primary is not treated as a terminal collision event. Instead, it is recorded as an auxiliary flag. This is why the plotted classifications include labels such as `okCOL0` and `ESCOL0`. In these labels, `COL0` denotes return to the regularized primary, while `COL1` denotes collision with the other primary. Thus:

`ok`	no escape or cross-primary collision before the horizon,
`okCOL0`	return to the regularized primary, but no terminal event,
`ESC`	escape without recorded self-return,
`ESCOL0`	escape after self-return to the regularized primary,
`COL1`	collision with the non-regularized primary,
`COL10`	cross-primary collision with an additional self-return flag,
`ERR`	Taylor integration error.

For the aggregate statistics, these composite labels are also grouped into broader categories:

`anyESC`,   `anyCOL0`,   `anyCOL1`.

This grouping separates escape, self-return, and cross-primary impact information while preserving the more detailed event history.

Stored Output

For each sampled initial condition, the code writes one row containing the regularization case, grid indices, event flag, closest approaches, event time, and reconstructed synodic state. The stored columns are

$$
\begin{aligned}
&\texttt{primary}, \quad \texttt{direction}, \quad i, \quad j, \quad \texttt{flag},\\
&d_{1,\min}, \quad \tau_{1,\min}, \quad d_{2,\min}, \quad \tau_{2,\min}, \quad \tau_{\text{event}},\\
&x, \quad y, \quad z, \quad \dot{x}, \quad \dot{y}, \quad \dot{z}.
\end{aligned}
$$

Here $d_{1,\min}$ and $d_{2,\min}$ are the minimum distances recorded to the two primaries during the integration, and $\tau_{1,\min}$ and $\tau_{2,\min}$ are the corresponding regularized times. The event time τ_{event} is the final integration time, either because a terminal event occurred or because the integration horizon was reached.

The final six entries are the reconstructed synodic position and velocity at the event or terminal time. These stored states make it possible to post-process cross-primary collisions and extract approximate ejection-collision connections. In the current version, the classification statistics use these rows primarily for counting and plotting. For a full-length version, the same output should also be used to construct tables of impact locations, arrival velocities, and Jacobi residuals at the detected cross-primary collision events.

Post-Processing

The raw output files are post-processed in two complementary ways.

The first post-processing step computes outcome percentages. For each fixed (C, p, d), the number of grid points in each event class is divided by the total number of sampled initial conditions. This gives the stacked percentage plots as functions of C. These plots are useful for identifying large-scale transitions, especially the loss of escape outcomes in the Moon-regularized branch as C approaches C_{L_2}.

The second post-processing step produces classification maps on the normalized ejection domain $(\sigma_1, \sigma_2) \in [0, 1]^2$. These maps retain the geometry of the initial-condition set and are more informative than percentages alone. In particular, the Moon-regularized maps show coherent escape regions, collision patches, and bounded regions rather than randomly scattered outcomes. This structure suggests that the observed transition is organized by invariant objects in the regularized phase space.

Mesh and Direction Comparisons

Two consistency checks are built into the numerical design.

First, the same classification problem is computed on both 64×64 and 128×128 grids. The 128×128 maps give sharper visual boundaries, while the 64×64 runs provide denser sampling in C near the transition. The two resolutions give the same qualitative result: Earth-regularized ejections remain bounded across the sampled range, while Moon-regularized ejections transition from escape-dominated to bounded as C increases.

Second, every case is computed in both time directions. The forward cases $d = +1$ and backward cases $d = -1$ show nearly identical aggregate statistics and very similar classification geometry. The small differences observed in the maps are mainly left-right rearrangements and finite-grid effects. This agreement provides a useful check that the transition is controlled primarily by the regularized primary and by C, not by the sign of the integration direction.

Summary of the Numerical Procedure

The full computational pipeline is therefore:

1. Choose the Jacobi constant C, regularized primary p, integration direction d, mesh size $N_1 \times N_2$, and numerical thresholds.
2. Generate the tensor-product Chebyshev grid on $[\pi/2, 3\pi/2] \times [0, \pi]$.
3. Convert each angular grid point into a KS ejection initial condition with $u = 0$ and $|v|^2 = K_p$.
4. Integrate the KS equations in regularized time using a variable-step Taylor method.
5. After each accepted step, reconstruct synodic position and velocity.
6. Monitor distances to the two primaries and the large-distance escape threshold.
7. Record cross-primary collision, escape, self-return, bounded-horizon, or integration-error flags.
8. Store minimum distances, event times, and reconstructed terminal states.
9. Post-process the output into aggregate percentages and classification maps.
10. Compare 64×64 and 128×128 meshes, and compare $d = +1$ and $d = -1$ runs for consistency.

This methodology produces both statistical and geometric information. The percentages identify the global change in behavior as C varies, while the maps reveal the structure of the corresponding regions on the KS ejection domain.

RESULTS

The Jacobi-constant sweep reveals a clear asymmetry between ejections from the two primaries. The aggregate statistics for the 128×128 computations are shown in Figure 5. For each value of C, each regularized primary p, and each integration direction d, the figure reports the percentage of initial conditions assigned to each terminal or composite event class. The same data are also grouped into the aggregate categories anyESC, $\mathrm{anyCOL0}$, and $\mathrm{anyCOL1}$ for the Moon-regularized branch.

For the Earth-regularized branch, $p = 1$, the outcome is nearly uniform over the sampled Jacobi range. Both forward and backward integrations are dominated by $\mathrm{okCOL0}$. Thus, within the integration horizon and event thresholds used here, ejections from the larger primary return to the regularized primary without triggering escape or cross-primary collision. No visible transition analogous to the Moon branch is detected in the Earth-regularized data.

The Moon-regularized branch, $p = 2$, shows a much richer dependence on C. At low Jacobi values, from $C = 2.70$ through approximately $C = 3.05$, the sampled ejection domain is dominated by escape outcomes, especially ESCOL0. Small but coherent cross-primary collision components, classified through COL1 or COL10 and included in $\mathrm{anyCOL1}$, are also present. As C increases, the escape set contracts and the return-dominated class $\mathrm{okCOL0}$ grows. By the intermediate values near $C = 3.10$ and $C = 3.15$, the classification maps show a mixed regime in which return regions occupy a substantial part of the ejection domain while residual escape components remain.

The sharpest part of the transition occurs near the exterior-neck threshold $C_{L_2} \approx 3.17216$. For the Moon-regularized branch, residual escape survives up to approximately $C = 3.171$ but is essentially absent by $C = 3.172$ in the present data. For $C \geq 3.172$, the sampled Moon ejection domain is almost entirely return-dominated. This behavior is consistent with the zero-velocity topology: as C approaches C_{L_2} from below, the exterior gateway near L_2 closes, and escape trajectories disappear from the sampled ejection set. Figure 6 shows this reorganization directly on the KS parameter domain. Between $C = 3.10$ and $C = 3.15$, broad return-dominated bands emerge inside an escape-dominated background. By $C = 3.171$, only tiny residual escape islands remain, and by $C = 3.172$ the Moon-forward branch is visually almost entirely $\mathrm{okCOL0}$.

The forward and backward integrations give nearly identical aggregate statistics. Small differences in the classification maps are mainly geometric rearrangements on the finite grid rather than changes in the global percentages. This agreement indicates that the observed transition is controlled primarily by the regularized primary and by the Jacobi constant, rather than by the sign of the integration direction.

Figure 7 gives a more detailed view of the Moon-regularized forward branch at selected low Jacobi values. Each row shows the classification map, the minimum distance $d_{\mathrm{other,min}}$ to the non-regularized primary, the impact speed $|\mathbf{v}|_{\mathrm{impact}}$ on the $\mathrm{anyCOL1}$ subset, and the corresponding regularized collision time τ_{COL1}. The last two columns are intentionally blank away from the $\mathrm{anyCOL1}$ set, since impact speed and collision time are only defined for initial conditions that reach the other primary. These diagnostics show that the cross-primary collision points are not randomly scattered across the ejection domain. Instead, they occur in localized regions with coherent variation in closest approach, impact speed, and collision time. This supports the interpretation that the cross-primary events are organized by the regularized phase-space geometry.

The 64×64 computations provide a useful consistency check. Although the lower-resolution maps are noisier on a cell-by-cell basis, they reproduce the same qualitative behavior observed in the 128×128 scans. The Earth-regularized branch remains return-dominated across the sampled range, while the Moon-regularized branch transitions from escape-dominated to return-dominated behavior as C increases toward C_{L_2}. The denser sampling in C near the transition confirms that the final loss of residual escape occurs in the interval around $C = 3.171$–3.172.

Overall, the results show that the KS ejection domain is partitioned into coherent outcome regions whose geometry changes systematically with the Jacobi constant. For the Earth-regularized branch, the partition is nearly uniform and return-dominated. For the Moon-regularized branch, the partition reorganizes strongly as the exterior gateway closes. The closest-approach and impact diagnostics further indicate that the cross-primary collision subsets contain structured information that can be used to identify and refine ejection-collision connection families.

Figure 5 should be read as the main statistical summary of the sweep, while Figure 7 provides the corresponding geometric and collision-diagnostic information on the KS parameter domain.

CONCLUSIONS

This work presents a KS-regularized Jacobi-constant survey of ejection-collision dynamics in the spatial Earth–Moon CR3BP. The regularized formulation converts primary collision into a smooth ejection manifold, allowing systematic sampling of near-primary directions and robust classification of their global outcomes. By combining this parametrization with Chebyshev grids and event-based post-processing, the survey gives both statistical and geometric information about bounded, escaping, self-returning, and cross-primary collision trajectories.

The results show a clear asymmetry between the two primaries. For the tested Jacobi values,

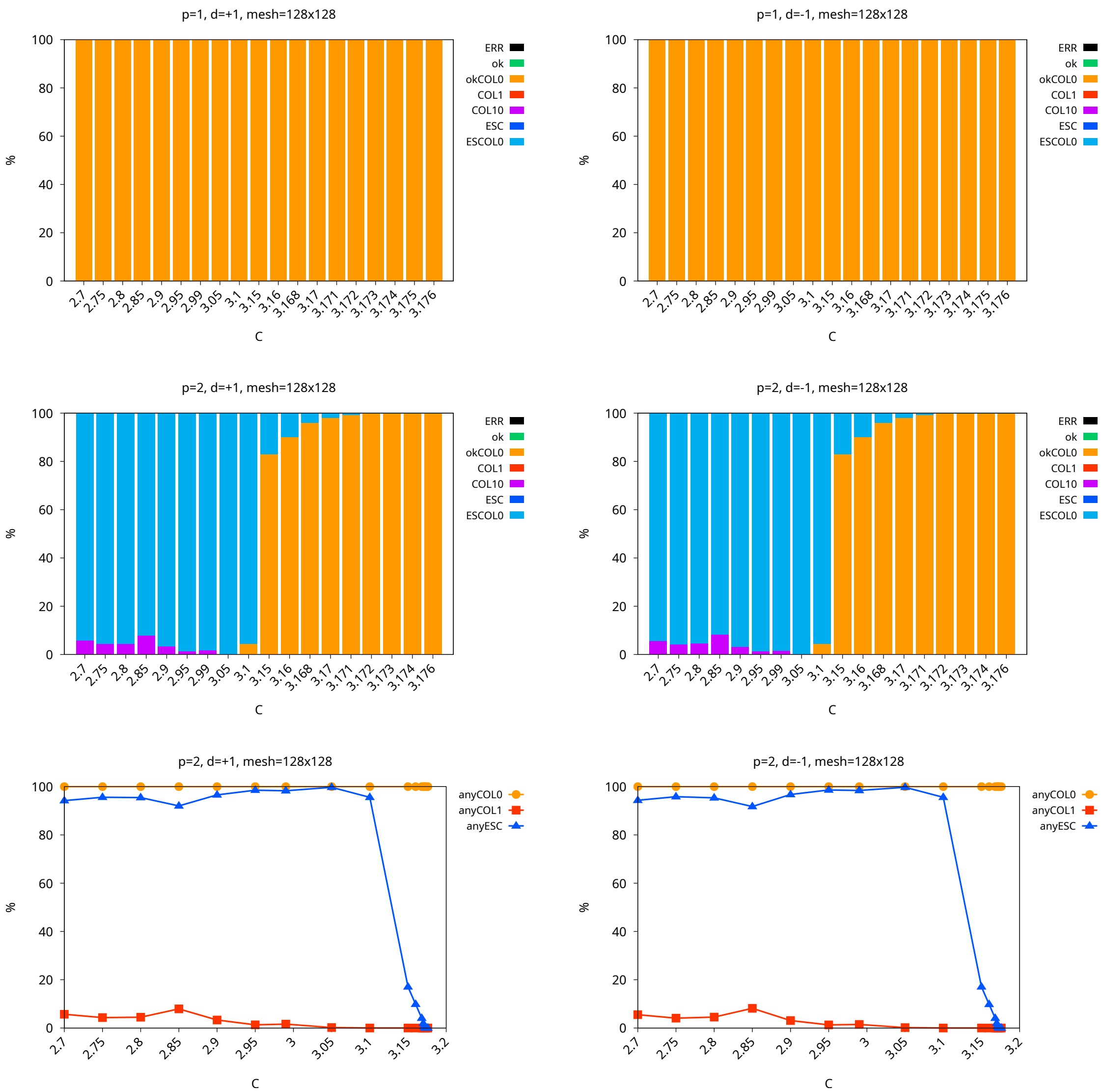

Figure 5. Outcome statistics for the 128×128 Jacobi-constant sweep. The top row shows Earth-regularized ejections, $p = 1$, for forward and backward integration; both directions are almost entirely classified as $\mathrm{okCOL0}$ over the sampled range, indicating return to the regularized primary without escape or cross-primary collision. The middle row shows Moon-regularized ejections, $p = 2$, where low-C cases are dominated by escape outcomes, mainly $\mathrm{ESCOL0}$, while increasing C produces a rapid transition to $\mathrm{okCOL0}$. The bottom row groups the Moon-regularized data into the aggregate event classes anyESC, $\mathrm{anyCOL0}$, and $\mathrm{anyCOL1}$, showing that escape trajectories disappear sharply near the exterior-neck threshold $C_{L_2} \approx 3.17216$. The denser 64×64 sweep confirms the same transition and locates the final loss of residual escape in the interval $C \approx 3.171$–3.172.

Earth-regularized ejections are dominated by return behavior to the regularized primary. Moon-regularized ejections display a pronounced transition: at lower C, escape outcomes occupy most of the sampled ejection domain, while near C_{L_2} the escape set rapidly contracts and the dynamics becomes return-dominated. This behavior is consistent with the closing of the exterior zero-velocity

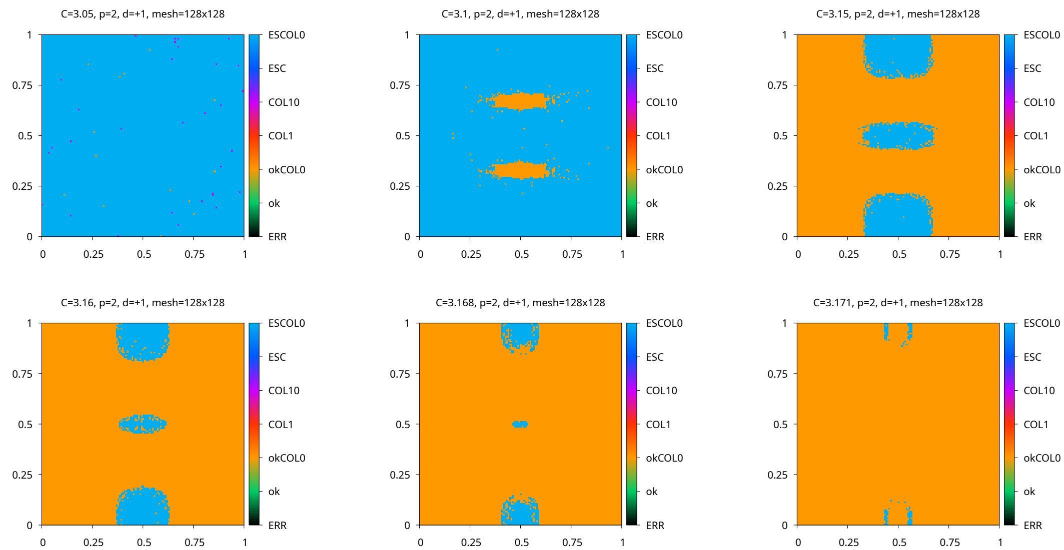

Figure 6. Moon-regularized forward classification maps, $p = 2$, $d = +1$, across the transition region. At $C = 3.10$ the domain is still escape-dominated, with return-rich horizontal bands already visible. After that, return dominates most of the domain and only structured residual escape caps and a narrow central band remain. The refined 64×64 sweep shows that these residual escape islands persist at $C = 3.171$ but are essentially absent by $C = 3.172$.

gateway near L_2 and demonstrates how global Hill-region topology is reflected in the regularized ejection manifold. The forward and backward integrations give nearly identical statistics and very similar classification maps, so the sign of time is secondary compared with the choice of regularized primary and the Jacobi constant. In the present Moon-regularized data, the final disappearance of residual escape occurs in the narrow interval $C \approx 3.171$–3.172.

The KS-domain maps reveal coherent regions of escape, return, and cross-primary collision. These structures persist across the sampled grids and time directions, indicating that the classification is organized by phase-space geometry rather than by random numerical scattering. The closest-approach, impact-speed, and collision-time diagnostics further show that the cross-primary collision sets contain structured information that can be used to locate and refine ejection-collision connection families.

The survey provides a useful foundation for continued studies of cislunar transport. Higher-resolution continuation of the observed regions, extraction of representative connection orbits, and extension to refined dynamical models can build directly on the present classification framework. In this sense, the KS-regularized ejection survey contributes to the broader dynamical understanding of Earth–Moon transport channels, including the near-Moon environment relevant to NRHO and Gateway-class cislunar operations.

ACKNOWLEDGMENT

The project has been supported by the Spanish grants PID2021-125535NB-I00 (MICINN/AEI/FEDER, UE), the Catalan grant 2021 SGR 01072, and by the Air Force Office of Scientific Research under award number FA8655-24-1-7059. The project that led to these results also received the support of a fellowship from “la Caixa” Foundation (ID 100010434), the fellowship code is LCF/BQ/PR23/11980047.

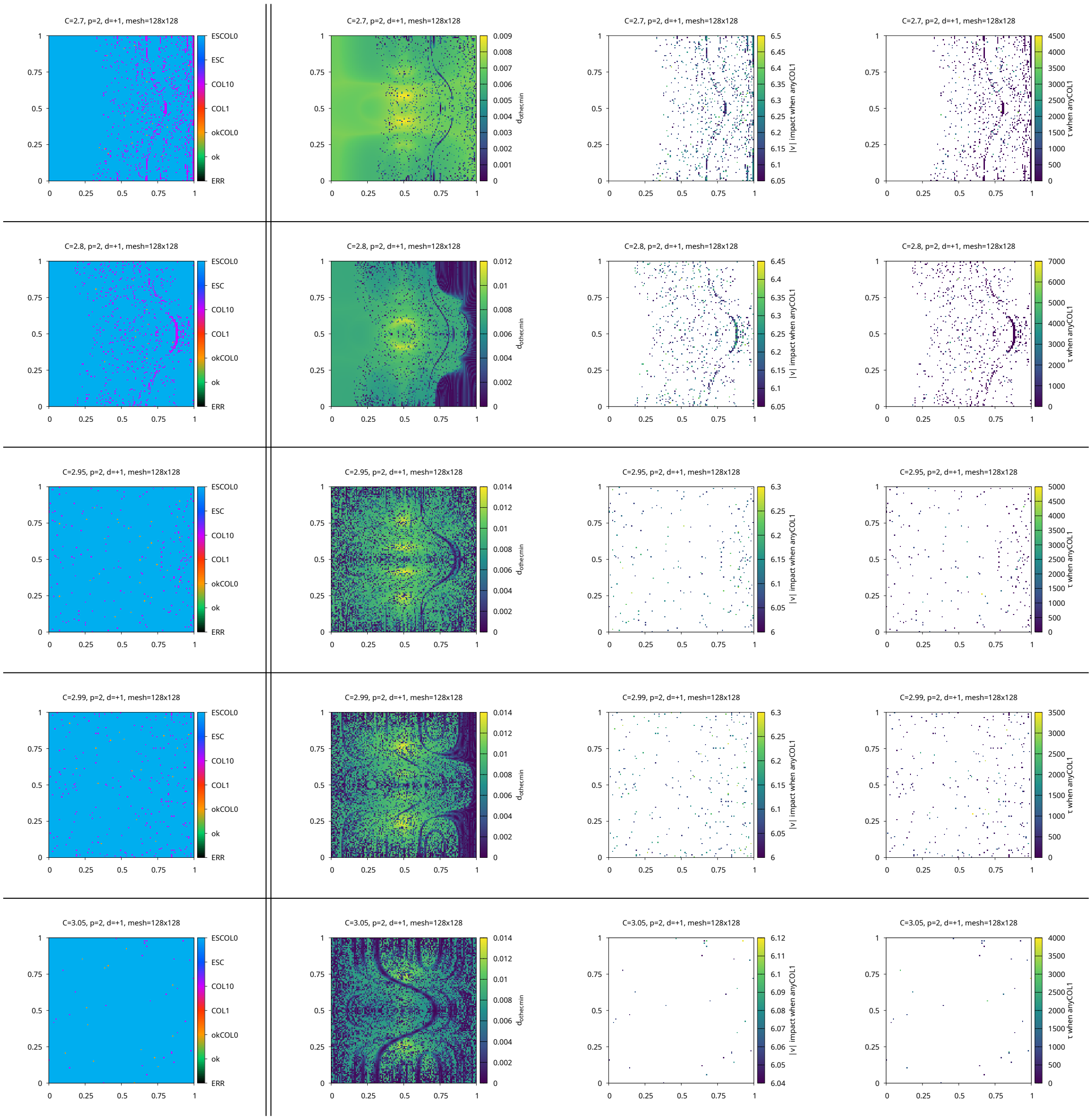

Figure 7. Moon-regularized classification and cross-primary collision diagnostics on the KS ejection domain. Each row corresponds to one Jacobi value, C, for the forward-time Moon-regularized branch, $p = 2$, $d = +1$, on a 128×128 grid. The first column gives the terminal outcome classification on the normalized Hopf-slice domain $(\sigma_1, \sigma_2) \in [0, 1]^2$. The second column shows the minimum distance $d_{\mathrm{other,min}}$ to the non-regularized primary, here the Earth, over the integration interval. The third and fourth columns restrict attention to initial conditions producing a cross-primary collision, $\mathrm{anyCOL1}$, and show respectively the reconstructed physical impact speed $|v|_{\mathrm{impact}}$ and the regularized collision time τ_{COL1}. Blank regions in the last two columns correspond to initial conditions that do not satisfy the $\mathrm{anyCOL1}$ condition. The coherent localization of the $\mathrm{anyCOL1}$ sets, together with the structured variation of closest approach, impact speed, and collision time, indicates that the cross-primary connections are organized by phase-space geometry rather than by random sampling effects.

NOTATION

μ	mass ratio (Moon/total),
M_1, M_2	larger (Earth) and smaller (Moon) primary
Ω	effective potential
C	Jacobi constant
C_{L_i}	Jacobi constant at Lagrangian point L_i
p	regularized primary index ($p = 1$ Earth, $p = 2$ Moon)
d	integration direction in regularized time (± 1)
τ	regularized time
$u, v \in \mathbb{R}^4$	KS position and velocities coordinates
$\mathcal{O}_i \cong S^3$	ejection sphere at primary M_i
θ_1, θ_2	Hopf-domain parameters on $\mathcal{O}_i$
σ_1, σ_2	normalized coordinates in $[0, 1]^2$
$g_{\mathtt{KS}}, E_{\mathtt{KS}}, R_{\mathtt{KS}}$	KS constraint and residual diagnostics
COL0	self-return to the regularized primary
COL1	collision with the non-regularized primary

REFERENCES

[1] V. Szebehely, *Theory of Orbits: The Restricted Problem of Three Bodies*. New York: Academic Press, 1967.

[2] W. S. Koon, M. W. Lo, J. E. Marsden, and S. D. Ross, "Dynamical systems, the three-body problem and space mission design," *Equadiff 99: (In 2 Volumes)*, pp. 1167–1181, World Scientific, 2000.

[3] C. C. Conley, "Low energy transit orbits in the restricted three-body problem," *SIAM Journal on Applied Mathematics*, Vol. 16, No. 4, 1968, pp. 732–746.

[4] G. Gómez, J. Llibre, R. Martínez, and C. Simó, *Dynamics and Mission Design Near Libration Points. Volume I: Fundamentals: The Case of Collinear Libration Points*, Vol. 2 of *World Scientific Monograph Series in Mathematics*. Singapore: World Scientific, 2001.

[5] G. Gómez, W.-S. Koon, M. W. Lo, J. E. Marsden, J. J. Masdemont, and S. D. Ross, "Invariant Manifolds, the Spatial Three-Body Problem and Space Mission Design," *Proceedings of the AAS/AIAA Astrodynamics Specialist Conference*, Quebec City, Canada, 2001. AAS 01-301.

[6] E. A. Belbruno and J. K. Miller, "Sun-perturbed Earth-to-Moon transfers with ballistic capture," *Journal of Guidance, Control, and Dynamics*, Vol. 16, No. 4, 1993, pp. 770–775.

[7] K. C. Howell and J. V. Breakwell, "Almost rectilinear halo orbits," *Celestial Mechanics*, Vol. 32, No. 1, 1984, pp. 29–52.

[8] NASA, "NRHO: The Artemis Orbit," `https://www.nasa.gov/wp-content/uploads/2023/10/nrho-artemis-orbit.pdf`. Accessed: 2026-07-07.

[9] NASA, "A Lunar Orbit That's Just Right for the International Gateway," `https://www.nasa.gov/centers-and-facilities/johnson/lunar-near-rectilinear-halo-orbit-gateway/`. Accessed: 2026-07-07.

[10] NASA, "CAPSTONE," `https://www.nasa.gov/mission/capstone/`. Accessed: 2026-07-07.

[11] P. Kustaanheimo and E. Stiefel, "Perturbation theory of Kepler motion based on spinor regularization," *Journal für die reine und angewandte Mathematik*, Vol. 218, 1965, pp. 204–219.

[12] E. L. Stiefel and G. Scheifele, *Linear and Regular Celestial Mechanics*. Berlin: Springer, 1971.

[13] P. Saha, "Interpreting the Kustaanheimo–Stiefel transform in gravitational dynamics," 2008. Preprint.

[14] J. Roa, H. Urrutxua, and J. Peláez, "Stability and chaos in Kustaanheimo–Stiefel space induced by the Hopf fibration," 2016. Preprint.

[15] M. Rossi and M. Guzzo, "A Kustaanheimo–Stiefel regularization of the elliptic restricted three-body problem and the detection of close encounters with fast Lyapunov indicators," 2022. Preprint.

[16] K. Oguri, "Regularization of the Circular Restricted Three-body Problem for Trajectory Optimization," *AAS/AIAA Astrodynamics Specialist Conference*, 2024, pp. 1–20.

[17] M. J. Capiński, S. Kepley, and J. Mireles James, "Computer Assisted Proofs for Transverse Collision and Near Collision Orbits in the Restricted Three Body Problem," *Journal of Differential Equations*, Vol. 366, 2023, pp. 132–191.

[18] J. Gimeno, J. D. Mireles James, and L. T. Peterson, "Ejection-Collision in the Spatial Restricted 3-Body Problem," Preprint, 2026.

[19] À. Jorba and M. Zou, "A software package for the numerical integration of ODEs by means of high-order Taylor methods," *Experimental Mathematics*, Vol. 14, No. 1, 2005, pp. 99–117.